Global Distribution of Three Types of Drop Size Distribution Representing Heavy Rainfall from GPM/DPR Measurements

Jihoon Ryu[1], Hwan-Jin Song[2], Byung-Ju Sohn[1,3], and Chao Liu[3,4]

[1]School of Earth and Environmental Sciences, Seoul National University, Seoul, Korea

[2]National Institute of Meteorological Sciences, Korea Meteorological Administration, Jeju, Korea

[3]Collaborative Innovation Center on Forecast and Evaluation of Meteorological Disasters, Nanjing University of Information Science & Technology, Nanjing 210044, China

[4]Key Laboratory for Aerosol-Cloud-Precipitation of China Meteorological Administration School of Atmospheric Physics, Nanjing University of Information Science & Technology, Nanjing 210044, China

Corresponding author: B.J. Sohn (sohn@snu.ac.kr)

Key Points:

- Global synthesis of drop size distributions for heavy rainfall using satellite-borne radar measurements.
- Three heavy rainfall types emerged – continental, oceanic deep, and oceanic shallow convective types.
- Geographic distributions of occurrence frequencies and rain contributions of three types are presented.

This article has been accepted for publication and undergone full peer review but has not been through the copyediting, typesetting, pagination and proofreading process, which may lead to differences between this version and the Version of Record. Please cite this article as doi: 10.1029/2020GL090871.

Abstract

In this study, Gaussian mixture model clustering analysis was carried out to examine characteristics of Global Precipitation Measurement (GPM) Dual-frequency Precipitation Radar (DPR)-retrieved mass-weighted mean diameter (D_m) and normalized intercept parameter (N_w) of the drop size distribution (DSD) for heavy rainfalls (> 10 mm h^{-1}) for six years (2014–19). Three objective DSD types – continental, oceanic deep, and oceanic shallow convective types – emerged. The means and standard deviations of D_m and N_w obtained for the three types are in good agreement with various ground-based observations, indicating that global view of DSD characteristics can be obtained from DPR-derived DSD parameters. Global distributions of occurrence and contribution of each DSD type to total heavy rainfall are produced for the first time, which will help examine the dominant DSD type, its contribution to total heavy rainfall, and composition of different convective types in the rainfall system at a given location.

Plain Language Summary

The surface rainfall is composed of a variety of spectrum of raindrops, which can be best represented by mean drop size and number concentration of droplets. Thus, those magnitude and shape may well describe rainfall-related features such as convective type and associated atmospheric environments. Thus, information on the rain drop size distribution is important for improving the remote sensing capability or modeling the rainfall phenomena. From the analysis of satellite-derived rain drop size distribution, it is noted that the heavy rainfall can be largely classified into three types – continental, oceanic deep, and oceanic shallow convective types. Satellite-derived mean diameter and drop size distribution for heavy rain are found to be very consistent with ground observations from limited local areas, indicating that the global view of

drop size distributions can be synthesized from the satellite observations. The newly obtained global features overcome the spatial limitations of existing studies using ground-based observations. Furthermore, estimated contribution to the heavy rainfall from each classified type shows that a largest portion is from the oceanic deep convective type, and the oceanic shallow convective type contributes as much as the continental type.

1. Introduction

The drop size distribution (DSD) of rainfall is important for estimating rain intensity and latent heating profiles using remote sensing data (Chapon et al., 2008; Liao et al., 2014; Nelson et al., 2016) and for parameterizing rain microphysics in numerical weather forecasting models (Lim & Hong, 2010; Zhang et al., 2006, 2008). It also helps in understanding and interpreting physical processes related to rain development (Chen et al., 2011). Thus, better understanding of its global characteristics can significantly advance our meteorological knowledge.

Previous DSD-related studies mainly used ground observations where the regional DSD characteristics were examined (Bringi et al., 2003; Dolan et al., 2018; Gatlin et al., 2015; Tang et al., 2014; Thompson et al., 2015; Ulbrich & Atlas, 2007; Zhang et al., 2020). Although these studies provided fundamental results by identifying DSD characteristics in various precipitation regimes, certain limitations exist when characteristics at any particular region is concerned, especially with regard to the understanding of rain processes over remote areas, such as in an open ocean. Furthermore, generalizing DSD characteristics has been challenging owing to the differences in the measuring instruments, study regions, time periods, and methodologies used in various studies. Thus, acquiring general characteristics applicable to any local area is necessary.

Satellite measurements seem to be an appropriate solution for examining such spatially and temporally varying DSD behaviors across diverse precipitation regimes.

Tropical Rainfall Measuring Mission (TRMM) was the first space-borne radar dedicated to rainfall measurement. The diameter parameter for DSD was retrieved using the precipitation radar (PR) measurements of reflectivity at a single Ku-band (13.8 GHz), assuming that the DSD can be characterized by the diameter parameter itself (Iguchi et al., 2000). However, as DSD variations cannot be fully expressed as a single parameter, rain rates (RRs) retrieved from single frequency radar measurements have often been found to prone to errors and biases (Iguchi et al., 2010).

Global Precipitation Measurement (GPM) satellite, a successor to TRMM, launched on February 27, 2014, carries a dual-frequency precipitation radar (DPR) and is much better at detecting DSDs as compared to the single band approach of PR (Iguchi et al., 2010). Difference between the radar reflectivities of the two frequencies (Ku-band: 13.60 GHz, Ka-band: 35.55 GHz) enables the retrieval of the two DSD parameters, mass-weighted mean diameter (D_m) and normalized intercept parameter (or normalized scaling parameter for concentration, N_w). This has enabled applications in different types of studies, for example, in the study of vertical structures of DSDs for stratiform and convective precipitation (Sun et al., 2020), microphysical features of tropical cyclones (Huang & Chen, 2019), and different DSD features between land and ocean (Kumar & Silva, 2019, Radhakrishna et al., 2016, 2020). Well-known features, such as difference between D_m of continental area and oceanic region was confirmed using globally retrieved DSD data (Seto et al., 2016; Yamaji et al., 2020). With large amount of accumulated data, comparing DPR-retrieved DSDs with in situ ground observations and understanding the comprehensive features of DSD across various rainfall regimes are more plausible. In particular, examining the

behavior of DSD characteristics in two-dimension carries significant importance. Note that in remote areas, such as open oceans or rain forest areas, which are presumably under different atmospheric environments, DSD features are difficult to obtain using the conventional disdrometer and polarimetric approaches.

In this study, we analyze the global DSD characteristics of heavy rainfall using multi-year DPR-retrieved DSDs and evaluate the remote sensing analysis results against ground observations provided in the literature. The obtained results can improve our understanding of cloud development and rain formation microphysics across global convection and rainfall regimes. This study can also further improve microphysical parameterizations needed for numerical models owing to the understanding of regionally different heavy rainfall microphysics.

2. Data and Methodology

In this study, GPM DPR-retrieved near-surface RR, D_m, N_w at clutter-free bottom level, and attenuation-corrected radar reflectivity profiles at the Ku-band (version 6) over the entire observation domain (65° N–65° S) during 2014–2019 are used (see Iguchi & Meneghini, 2016, 2017 for detailed DPR-retrieved parameters). Solid or mixed precipitation is not considered as the focus here is rain precipitation. We use the inner swath data of the matched scan mode where reflectivities are measured at both the Ku- and Ka-bands.

For the initial version of DPR-retrieved DSD data, it has been reported that the uncertainty is high for RR > 8 mm h^{-1} cases, compared to the disdrometer measurements over Gadanki, India (Radhakrishna et al., 2016). From the validation of the updated version 4 data over the Mediterranean region, D'Adderio et al. (2019) reported that probability distribution of DPR-retrieved D_m is well matched with disdrometer measurements, but logN_w is subject to uncertainties.

For the latest version (i.e., version 6), agreement is good between retrievals and disdrometer measurements over the central China for Meiyu monsoon events; correlation coefficient is higher than 0.6 with no significant mean bias (Sun et al., 2020), satisfying the DSD measurement requirement of 0.5 mm error range for the GPM mission (Skofronick-Jackson et al., 2017). Indirect validation of was undertaken about the microphysical assumption used for the DSD retrievals (version 6), using disdrometer measurements from numerous NASA's Ground Validation (GV) field campaign sites over the United States and Department of Energy-Atmospheric Radiation Measurement (DOE-ARM) mobile facility deployments over the globe (Chase et al., 2020). It was demonstrated that employed microphysical assumption of rain-drop size relationship for the rain is in good agreement with disdrometer measurements, further assuring the quality of version 6 DPR-retrieved DSD retrievals.

The DSD function for raindrops (N(D)) is normally described by the gamma distribution function (Ulbrich, 1983) and its normalized form (Testud et al., 2001) can be written as follows:

$$N(D) = N_w \frac{6}{4^4} \frac{(4+\mu)^{\mu+4}}{\Gamma(\mu+4)} \left(\frac{D}{D_m}\right)^{\mu} \exp\left[-(4+\mu)\frac{D}{D_m}\right] \qquad (1)$$

where μ, D, and N(D) are the shape parameter, diameter bin in mm, and number concentration in $mm^{-1}m^{-3}$. D_m is the mass-weighted mean diameter in mm, and N_w is the normalized intercept parameter in $mm^{-1}m^{-3}$. In this study, the shape parameter $\mu = 3$ is used as in other studies (Liao et al., 2014; Seto et al., 2013). By using the values of D_m and N_w retrieved from DPR measurements, the corresponding number concentration N(D) is calculated using Eq. (1).

The procedures for data construction needed for examining the global DSD characteristics are shown in Figure S1. We first define an equal-area grid, equivalent to the 5° × 5° grid area over

an equatorial region such that the number of heavy rain pixels and corresponding D_m and N_w values can be saved at each equal-area grid. If there exist more than one pixel showing the RR greater than 10 mm h^{-1} at a given equal-area grid (about 5° × 5° area at the equator), the grid is considered to have a heavy rain event. An RR of 10 mm h^{-1} exhibits a threshold separating the stratiform rain type from the convective one (Tokay & Short, 1996). Subsequently, the D_m, N_w, and RR data of all heavy rain pixels at a given grid and time are constructed. After repeating the data constructing procedure over the entire domain and analysis period, we construct a raw dataset containing the D_m, N_w, and RR of all the heavy rain pixels over the 65° N–65° S observation domain and six year period (2014–2019). However, considering the high visiting frequency of the GPM satellite in higher latitudes, the raw dataset will have a bias of more samplings in higher latitudes. Samplings are therefore homogenized to construct the final dataset that is used for the clustering analysis. After counting the visiting frequency of the satellite depending on the latitude, the number of samples for each latitude are scaled using the ratio of the visiting frequency at each latitude to the visiting frequency at the equator. Afterwards, heavy rain events at a given latitude are randomly selected to equate the scaled number at the latitude to reduce uneven sampling problem. As a result, 328,391 heavy rain events (or number of grids showing heavy rain) and 6,258,800 heavy rain pixels over the study domain are collected for analysis. Finally, heavy rain pixels within a grid are averaged to yield mean D_m and $\log N_w$ for that specific grid. The constructed data of D_m and $\log N_w$ for heavy rain events are used for classifying the DSD types based on Gaussian mixture model (GMM; Bishop, 2006). GMM is a statistical model that is used to group the sample data into clusters assuming the presence of a certain number of Gaussian distributions in the sample data. Thus, each classified type best satisfies its own Gaussian distribution with associated mean and

standard deviation. Details on how classification was carried using GMM are found in the Supplementary Information.

3. Results

3.1. Three classified DSD types

For classifying the DSD types, we examine whether the constructed D_m and $\log N_w$ satisfy the Gaussian distributions for estimating the applicability of GMM. The distributions of D_m and $\log N_w$ were found be similar to Gaussian distributions (not presented). The number of classified types can be subjective, but the types must be consistent with known meteorological features. Three types appear most relevant when the DSD characteristics and associated geographical features are estimated.

Figure 1a–c show the frequency distributions of D_m and $\log N_w$ for the three heavy rainfall types classified using GMM. It can be seen that D_m reduces from Type 1 to Type 3, whereas $\log N_w$ increases. The mean ± standard deviations for D_m for the three types are 2.25 ± 0.49, 1.62 ± 0.34, and 1.25 ± 0.27 mm, respectively and corresponding $\log N_w$ mean ± standard deviations are 3.49 ± 0.49, 4.15 ± 0.45, and 4.64 ± 0.47 m^{-3} mm^{-1}. D_m for Type 1 exhibits a high frequency at 3 mm because the maximum value for D_m retrieved from the DSD algorithm was set to 3 mm (Seto et al., 2016). As the DSD types of heavy rainfall are classified based on the frequency histograms of the events, the range of one standard deviation between Type 1 (Type 2) and Type 2 (Type 3) overlaps by 9.5% (17.0%).

To obtain the DSD distributions corresponding to the three D_m-$\log N_w$ types, the respective D_m and $\log N_w$ values are inserted in Eq. (1), given $\mu = 3$. Obtained results are given in Figure 1d–f. As a form of gamma function, the number concentration increases until a certain diameter (i.e.,

an inflection point) and subsequently decreases. The diameters at the inflection points for the three types are 1.0, 0.6, and 0.4 mm. The number concentration around these diameters appears lowest for Type 1 and highest for Type 3. In contrast, toward the larger diameter side (e.g., D > 3 mm), Type 1 shows the highest number concentration, whereas Type 3 shows the lowest. However, Type 2 and Type 3 resemble each other. Geographical distributions of D_m and $\log N_w$ that support the description provided in Figure 1 are displayed in Supplementary Figure S2.

DSD at the surface should be closely linked to the vertical structure of the cloud system. In this study, we examine vertical structures of clouds for three DSD types. For this, the frequency of Ku-band radar reflectivity is provided in the reflectivity-height coordinates (Figure 1g-i). It is indicated that the cloud develops highest for Type 1 and lowest for Type 3, suggesting the strongest convection intensity for Type 1 and weakest for Type 3. Compared with the normalized distributions of the storm height for three types (Figure S3), showing the minimum reflectivity at approximately 12–15 dBz (Hamada & Takayabu, 2016) highest for Type 1 and lowest for Type 3, the surface mean reflectivity seems to be proportional to the storm height as well as convection strength. The vertical shapes of reflectivity for first two types given in Figure 1g-i are consistent with the results of previous studies on precipitation characteristics representing continental and oceanic types (Liu et al., 2007; Liu et al., 2008; Hamada et al., 2015; Sohn et al., 2013; Song & Sohn, 2015; Xu & Zipser, 2012; Zipser et al., 2006).

The diurnal variations in convective rainfall have been well-established to be distinctly different between continents and oceans; maximum precipitation over continents and oceans occur at 15–18 and 03–06 LST, respectively (Liu & Liu, 2016; Liu & Zipser, 2008; Nesbitt and Zisper, 2003; Song & Sohn, 2015; Takayabu, 2002; Yang & Smith, 2006; Zipser et al., 2006). The diurnal variations for DSD Type 1 and Type 2 are similar to those noted for the continent and ocean (Figure

S4). Thus, the DSD characteristics for Type 1 and 2 should represent the continental and oceanic types of heavy precipitation, respectively. Type 3 shows similar variations to Type 2, but with smaller amplitudes.

3.2. Global distributions of three classified DSD types

The spatial distributions of occurrence frequencies and volumetric heavy rainfalls associated with each DSD type can be drawn and the dominant DSD types can be examined from this at any given location of the domain (Figure 2). Compared to surface-based DSD studies conducted at limited regions, which provided the most dominant DSD features, this study provides information related to a combination of DSD types or the dominant DSD type at any given location. Type 1 shows a relatively high frequency in Africa, Europe, US and South America, and western Pacific maritime continent, thereby confirming that Type 1 rainfall is mostly the continental type (Figure 2a).

Type 2 shows the dominant occurrence frequency for heavy rainfall over the tropical oceanic regions. Southeast Asian and east Asian monsoon regions as well as north Atlantic Ocean also show a prevalent Type 2 rainfall. Thus, Type 2 mainly represents the ocean type. It should also be noted that the Amazon rainforests fall into oceanic Type 2, with a less frequent continental Type 1 also evident in these forests. The dominant ocean type behaviors of rainfall over the Amazon have been well recognized in previous studies (Williams et al., 2002; Zipser et al., 2006).

Geographical distributions of Type 3 (Figure 2e) mostly overlap with Type 2, indicating that oceanic convections causing heavy rainfall comprise of deep as well as shallow convection. Thus, heavy rainfall over the ocean regions may be characterized by a bimodal distribution with two main modes of Type 2 and Type 3, with Type 2 being the dominant one. Despite the overlapping tendency of Type 3 with Type 2, the main locations for Type 3 are toward the

subtropical high regions off the dominant regions for Type 2, except the equatorial eastern Pacific region where Type 3 is also prevalent.

Obtained results of D_m and $\log N_w$ for three DSD types are found to be consistent with known microphysical processes of precipitation. In the continental regions where Type 1 occurs most frequently, it is well known that abundant ice particles including graupel and hail are present in clouds due to the strong convection. Such clouds generally produce larger raindrops at the surface, after experiencing the melting and collision-coalescence processes (Cecil, 2011; Cecil et al., 2012; Liu et al., 2008; Sohn et al., 2015; Xu & Zipser, 2012; Zipser et al., 2006 among many others). Thus, larger raindrop sizes (and smaller number concentration) found in this study are consistent with general rain characteristics found over the land. In tropical oceanic regions where Type 2 is dominant, ice water content is relatively small (Cecil, 2011; Sohn et al., 2015) while liquid water content is abundant (Wood et al., 2002), in comparison to the land type. With the convection intensity weaker than the land type, collision-coalescence processes are known to be the main rain growing physics (Xu & Zipser, 2012), resulting in drop sizes smaller than the land type. The Type 3 mostly found over the subtropical subsidence region and equatorial eastern Pacific appears to be largely associated the warm rain processes under weaker and shallow convection, giving relatively lower cloud top, smaller drop size, and larger number concentration (Liu et al., 2008; Sekaranom & Masunaga, 2019; Xu & Zipser, 2012).

In this study, we examine the rainfall amount at each grid contributed by each DSD type. For this, the volumetric heavy rainfall is calculated at each grid by summing all the selected pixel-level RRs within the grid. Results are shown in Figure 2b, d, and f. It can be seen that 63.5% of the total rainfall is contributed by Type 2, which is predominantly from oceans. Another 18.3% of the total heavy rainfall is contributed by Type 3, mostly over the oceans as well, and the remaining

18.2% of the total heavy rainfall is contributed by Type 1 mostly over the land regions. Again, the eastern Pacific ITCZ area show nearly compatible amounts of heavy rainfalls from both Type 2 and Type 3. Overall, the spatial distribution analysis mentioned above brought a conclusion that Type 1, Type 2, and Type 3 should be linked to continental convection, oceanic deep convection, and oceanic shallow convection, respectively.

We also examine the seasonally varying occurrence frequencies and volumetric rains for the three aforementioned types. In the boreal summer, occurrence frequency and volumetric heavy rainfall for the continental type occurred for most continents in the Northern Hemisphere, except Sahara and Arabia desert regions (Figure S5a–b). Regions showing oceanic deep and shallow convective types move to the north compared to the distribution of annual mean (Figure S5c–f). Contrastingly, in the boreal winter, the continental type is most commonly found in the Southern Hemispheric land regions, whereas the oceanic type is most commonly found in the Indo-western Pacific Oceans and Amazon area (Figure S6c–f). Despite the seasonally varying geographical distributions of occurrence frequencies and volumetric rains, the results obtained for annual means of DSD parameters, as depicted in Figure 1, are found to be persistent.

3.3. Comparison with ground-based DSD observations

These globally classified DSD types are important to comprehensively interpret the DSD results of previous studies that have often represented local/regional characteristics. The global mean D_m and $\log N_w$ values for the three types (Figure 1) are compared with the results of previous studies (Figure 3 and Table S1). Note that heavy rains as presented in Table S1 represent the cases with rain rates stronger than 10 mm h^{-1} (as observed in this study), whereas convective rains represent the cases with rain rates higher than 5 mm h^{-1} and standard deviations greater than 1.5 mm h^{-1} observed over a certain time period (Bringi et al., 2003).

The values of D_m and $\log N_w$ of the continental convective type (2.25 ± 0.49 mm and 3.49 ± 0.49 m^3 mm^{-1}, respectively) are consistent within a one standard deviation, based on the results obtained from Colorado US, Austria, Sydney Australia, and Puerto Rico (Bringi et al., 2003), the United Kingdom and Greece (Montopoli et al., 2008), northern China (Chen et al., 2016), and Tibetan Plateau (Chen et al., 2017). Furthermore, the values of D_m and $\log N_w$ of the oceanic deep convective type (1.62 ± 0.34 mm and 4.15 ± 0.45 m^3 mm^{-1}, respectively) are found to be in good agreement with the results obtained from India (Lavanya et al., 2019; Radhakrishna et al., 2020), Indonesia (Marzuki et al., 2013), southern China (Huo et al., 2019; Sun et al., 2020), Taiwan (Seela et al., 2018), South Korea (Suh et al., 2016), Japan (Montopoli et al., 2008), Darwin Australia, Papua New Guinea (Bringi et al., 2003), western Pacific (Bringi et al., 2003; Huang & Chen, 2019), and Amazon regions (Bringi et al., 2002). These maritime and monsoon regions are located in the areas showing features of the oceanic deep convective type. Notably, the D_m and $\log N_w$ distributions for the oceanic deep convective type overlap with those of the oceanic shallow convective type (Figure 1b-c, and Figure 3). However, ground-based results showing the oceanic shallow convective type DSD distribution are rare except for the DSD distributions of typhoons that made landfalls in China (Wen et al., 2018) and India (Janapati et al., 2017; Janapati et al., 2020). The typhoon generally shows features of the oceanic shallow convective type, but seems to depend on the location or development stage (Janapati et al., 2020). The lack of observations associated with the oceanic shallow convective type is likely due to the fact that this type is mostly found over the open oceans near the subtropical subsidence regions, equatorial eastern Pacific, and equatorial Atlantic Ocean.

These classified types are also in good agreement with three DSD groups for convective precipitation based on ground-based disdrometer measurements covering diverse meteorological

regimes from the tropics to the high latitudes (Dolan et al., 2018); Type 1, 2, and 3 are very similar to their 'ice-based convection', 'warm rain with high liquid water content', and 'weak convective warm rain shower' groups. Since the comparison of the classified results with ground-based measurements should be an indirect validation of DPR DSD products, the close agreement of classified rain types with results from ground-based measurements further assures the DPR-retrieved data quality and obtained results.

4. Conclusions and discussion

In this study, we examined the global characteristics of two DSD parameters of heavy rainfall (> 10 mm h^{-1}), D_m, and N_w for six years (2014–2019) of GPM DPR estimates over the 65°N–65°S observation domain. Three typical DSD types were identified in this study. The first type (continental convective type) with the largest D_m and lowest $\log N_w$ mainly prevails over continental regions, accounting for approximately 26.3% and 18.2% of the global heavy rain events and total heavy rainfall, respectively. The six-year mean and associated standard deviations of D_m and $\log N_w$ (2.25 ± 0.49 mm and 3.49 ± 0.49 m^{-3} mm^{-1}, respectively) obtained in this study are in good agreement with the continental-like cluster found globally in ground-based observations. The second type (oceanic deep convective type) showing medium values of D_m and $\log N_w$ is mostly found over tropical oceans and humid monsoon areas. Results indicate that approximately 63.5% of the total heavy rainfall was contributed by this type. The means and standard deviations of D_m and $\log N_w$ (1.62 ± 0.34 mm and 4.15 ± 0.45 m^{-3} mm^{-1}, respectively) are also in good agreement with the surface observations of maritime-like cluster reported. The third type (oceanic shallow convective type) is also found to be of the ocean type, but is associated with shallow convection, covering 18.3% of the total heavy rainfall, approximately same as that in the case of the continental convective type (18.2%). Despite the occurrence area being mostly

overlapped with the second type, the maximum occurrence regions are found along the ITCZ over the equatorial Pacific and Atlantic Ocean and over regions near subtropical highs. The smallest D_m and highest $\log N_w$ (1.25 ± 0.27 mm and 4.65 ± 0.47 m^{-3} mm^{-1}, respectively) are found in this type of heavy precipitation.

Results from this study are important because the DSD characteristics of heavy rainfall in any region can be interpreted as a combination of different DSD types with origins closely associated with the cloud-scale processes and environments. Furthermore, the global distributions of means and standard deviations of D_m and $\log N_w$ for the three types, associated distributions of the occurrence of each type, and contribution to total heavy rainfall will help in understanding the physical processes of heavy rain formation, particularly over remote areas, such as open oceans where conventional observations cannot be readily made.

In spite of classification results compromising overall DSD features noted over the globe, we admit caveats of statistically-based DSD classifications. The same resultant DSD type could be attributed to many different physical reasonings responsible for the rain. For example, if there are dominant breakup processes over the continent, then DSD types without physical consideration may be interpreted as an ocean type although physical processes responsible for the ocean type can be quite different from the continental type. Thus, more future studies are needed for better understanding of the precipitation microphysics, especially combined with regionally-based physical processes such as collision and breakup processes, water vapor convergence, aerosol loadings, and so on.

While main discussions in this study have been made for interpreting three classified DSD types and their geographical distributions, obtained results can further envision studying climate change features, validating climate models, and improving cloud microphysical parameterization.

For example, results obtained in this study may allow us to examine how two oceanic types of rainfall revealed in this study respond to changes in tropical circulations over the Pacific such as Walker circulation. And separated rain types and their contributions to the total rainfall can be used for the validation of climate model simulations, which should be more useful than the simple total rainfall comparison. The obtained results may also provide more insights on how specific rain types are linked to specific cloud structures at a given area. It is because precipitation cannot be separated from cloud microphysics.

Acknowledgments and Data

The GPM products (2ADPR and 2AKu) were obtained from the NASA/Goddard Space Flight Center's science team and PPS (https://storm.pps.eosdis.nasa.gov/storm/). We appreciate Prof. Ed Zipser and two anonymous reviewers for providing constructive comments which surely led to an improved paper. Special thank is given to Prof. Shinta Seto at Nagasaki University for providing detailed information regarding the DPR algorithm. This work was funded by NRF-2020R1A2C1007005. HJS was supported by the KMA R&D Grant (KMA2018-00124), and CL was supported by the National Key Research and Development Program of China (2018YFC1506502).

References

Bishop, C. M. (2006). *Pattern recognition and machine learning*, Springer, New York.

Bringi, V. N., Chandrasekar, V., Hubbert, J., Gorgucci, E., Randeu, W. L., & Schoenhuber, M. (2003). Raindrop size distribution in different climatic regimes from disdrometer and dual-polarized radar analysis. *Journal of the Atmospheric Sciences, 60*(2), 354–365. https://doi.org/10.1175/1520-0469(2003)060<0354:RSDIDC>2.0.CO;2.

Bringi, V. N., Haung, G. J., Chandrasekar, V., & Gorgucci, E. (2002). A methodology for estimating the parameters of a gamma raindrop size distribution model from polarimetric radar data: A

application to a squall-line event from the TRMM/Brazil campaign. *Journal of Atmospheric and Oceanic Technology, 19*(5), 633–645. https://doi.org/10.1175/1520-0426(2002)019<0633:AMFETP>2.0.CO;2.

Cecil, D. J. (2011). Relating passive 37-GHz scattering to radar profiles in strong convection. *Journal of Applied Meteorology and Climatology, 50*(1), 233-240. https://doi.org/10.1175/2010JAMC2506.1.

Cecil, D. J., & Blankenship, C. B. (2012). Toward a global climatology of severe hailstorms as estimated by satellite passive microwave imagers. *Journal of Climate, 25*(2), 687-703. https://doi.org/10.1175/JCLI-D-11-00130.1.

Chapon, B., Delrieu, G., Gosset, M., & Boudevillain, B. (2008). Variability of rain drop size distribution and its effect on the Z–R relationship: A case study for intense Mediterranean rainfall. *Atmospheric Research, 87*(1), 52-65. https://doi.org/10.1016/j.atmosres.2007.07.003.

Chase, R. J., Nesbitt, S. W., & McFarquhar, G. M. (2020). Evaluation of the microphysical assumptions within GPM-DPR using ground-based observations of rain and snow. *Atmosphere, 11*(6), 619. https://doi.org/10.3390/atmos11060619.

Chen, B., Hu, Z., Liu, L., & Zhang, G. (2017). Raindrop size distribution measurements at 4,500 m on the Tibetan Plateau during TIPEX-III. *Journal of Geophysical Research: Atmospheres, 122*(20), 11092–11106. https://doi.org/10.1002/2017JD027233.

Chen, B., Hu, W., & Pu, J. (2011). Characteristics of the raindrop size distribution for freezing precipitation observed in southern China. *Journal of Geophysical Research: Atmospheres, 116*(D6). https://doi.org/10.1029/2010JD015305.

Chen, B., Wang, J., & Gong, D. (2016). Raindrop size distribution in a midlatitude continental squall line measured by Thies optical disdrometers over East China. *Journal of Applied Meteorology and Climatology, 55*(3), 621–634. https://doi.org/10.1175/JAMC-D-15-0127.1.

D'Adderio, L. P., Porcù, F., Panegrossi, G., Marra, A. C., Sanò, P., & Dietrich, S. (2019). Comparison of the GPM DPR single- and double-frequency products over the Mediterranean area. *IEEE Transactions on Geoscience and Remote Sensing, 57*(12), 9724-9739. https://doi.org/10.1109/TGRS.2019.2928871.

Dolan, B., Fuchs, B., Rutledge, S. A., Barnes, E. A., & Thompson, E. J. (2018). Primary modes of global drop size distributions. *Journal of the Atmospheric Sciences, 75*(5), 1453–1476. https://doi.org/10.1175/JAS-D-17-0242.1.

Gatlin, P., Thurai, M., Bringi, V. N., Petersen, W., Wolff, D., Tokay, A., et al. (2015). Searching for large raindrops: A global summary of two-dimensional video disdrometer observations. *Journal of Applied Meteorology and Climatology, 54*(5), 1069–1089, https://doi.org/10.1175/JAMC-D-14-0089.1.

Hamada, A., & Takayabu, Y. N. (2016). Improvements in detection of light precipitation with the Global Precipitation measurement dual-frequency precipitation radar (GPM DPR). *Journal of Atmospheric and Oceanic Technology, 33*(4), 653–667. https://doi.org/10.1175/JTECH-D-

15-0097.1.

Hamada, A., Takayabu, Y. N., Liu, C., & Zipser, E. J. (2015). Weak linkage between the heaviest rainfall and tallest storms. *Nature Communications, 6*, 6213. https://doi.org/10.1038/ncomms7213.

Huang, H., & Chen, F. (2019). Precipitation microphysics of tropical cyclones over the western North Pacific based on GPM DPR observations: A preliminary analysis. *Journal of Geophysical Research: Atmospheres, 124*(6), 3124–3142. https://doi.org/10.1029/2018JD029454.

Huo, Z., Ruan, Z., Wei, M., Ge, R., Li, F., & Ruan, Y. (2019). Statistical characteristics of raindrop size distribution in south China summer based on the vertical structure derived from VPR-CFMCW. *Atmospheric Research, 222*, 47–61. https://doi.org/10.1016/j.atmosres.2019.01.022.

Iguchi, T., & Meneghini, R. (2016). GPM DPR Ku Precipitation Profile 2A 1.5 hours 5 km V06, Greenbelt, MD, Goddard Earth Sciences Data and Information Services Center (GES DISC). https://doi.org/10.5067/GPM/DPR/Ku/2A/06.

Iguchi, T., & Meneghini, R. (2017). GPM DPR Precipitation Profile L2A 1.5 hours 5 km V06, Greenbelt, MD, Goddard Earth Sciences Data and Information Services Center (GES DISC). https://doi.org/10.5067/GPM/DPR/GPM/2A/06.

Iguchi, T., Kozu, T., Meneghini, R., Awaka, J., & Okamoto, K. I. (2000). Rain-profiling algorithm for the TRMM precipitation radar. *Journal of Applied Meteorology*, *39*(12), 2038-2052. https://doi.org/10.1175/1520-0450(2001)040<2038:RPAFTT>2.0.CO;2.

Iguchi, T., Seto, S., Meneghini, R., Yoshida, N., Awaka, J., Le, M., et al. (2010). GPM/DPR level 2 algorithm theoretical basis document, *Technical Report*. [Available at https://gpm.nasa.gov/sites/default/files/document_files/ATBD_DPR_201811_with_Appendix3b_0.pdf].

Janapati, J., Reddy, V., Reddy, K., Lin, P. L., & Liu, C. Y. (2017). A study on raindrop size distribution variability in before and after landfall precipitations of tropical cyclones observed over southern India. *Journal of Atmospheric and Solar-Terrestrial Physics*, *159*, 23-40. https://doi.org/10.1016/j.jastp.2017.04.011.

Janapati, J., Seela, B. K., Lin, P.-L., Wang, P. K., Tseng, C.-H., Reddy K. K., et al. (2020). Raindrop size distribution characteristics of Indian and Pacific Ocean tropical cyclones observed at India and Taiwan Sites. *Journal of the Meteorological Society of Japan. Ser. II., 98*(2), 299–317. https://doi.org/10.2151/jmsj.2020-015.

Kumar, S., & Silva, Y. (2019). Vertical characteristics of radar reflectivity and DSD parameters in intense convective clouds over South East South Asia during the Indian summer monsoon: GPM observations. *International Journal of Remote Sensing, 40*(24), 9604–9628. https://doi.org/10.1080/01431161.2019.1633705.

Lavanya, S., Kirankumar, N. V. P., Aneesh, S., Subrahmanyam, K. V., & Sijikumar, S. (2019).

Seasonal variation of raindrop size distribution over a coastal station Thumba: A quantitative analysis. *Atmospheric Research, 229*, 86-99. https://doi.org/10.1016/j.atmosres.2019.06.004.

Liao, L., Meneghini, R., & Tokay, A. (2014). Uncertainties of GPM DPR rain estimates caused by DSD parameterizations. *Journal of Applied Meteorology and Climatology, 53*(11), 2524–2537. https://doi.org/10.1175/JAMC-D-14-0003.1.

Lim, K. S. S., & Hong, S. Y. (2010). Development of an effective double-moment cloud microphysics scheme with prognostic cloud condensation nuclei (CCN) for weather and climate models. *Monthly Weather Review, 138*(5), 1587–1612. https://doi.org/10.1175/2009MWR2968.1.

Liu, N., & Liu, C. (2016). Global distribution of deep convection reaching tropopause in 1 year GPM observations. *Journal of Geophysical Research: Atmospheres, 121*(8), 3824–3842. https://doi.org/10.1002/2015JD024430.

Liu, C., & Zipser, E. J. (2008). Diurnal cycles of precipitation, clouds, and lightning in the tropics from 9 years of TRMM observations. *Geophysical Research Letters, 35*(4). L04819. https://doi.org/10.1029/2007GL032437.

Liu, C., Zipser, E. J., Cecil, D. J., Nesbitt, S. W., & Sherwood, S. (2008). A cloud and precipitation feature database from nine years of TRMM observations. *Journal of Applied Meteorology and Climatology, 47*(10), 2712–2728. https://doi.org/10.1175/2008JAMC1890.1.

Liu, C., Zipser, E. J., & Nesbitt, S. W. (2007). Global distribution of tropical deep convection: Different perspectives from TRMM infrared and radar data. *Journal of Climate, 20*(3), 489–503. https://doi.org/10.1175/JCLI4023.1.

Marzuki, M., Hashiguchi, H., Yamamoto, M. K., Mori, S., & Yamanaka, M. D. (2013). Regional variability of raindrop size distribution over Indonesia. *Annales Geophysicae, 31*(11), 1941–1948. https://doi.org/10.5194/angeo-31-1941-2013.

Montopoli, M., Marzano, F. S., Vulpiani, G., Anagnostou, M. N., & Anagnostou, E. N. (2008). Statistical characterization and modeling of raindrop spectra time series for different climatological regions. *IEEE Transactions on Geoscience and Remote Sensing, 46*(10), 2778–2787. https://doi.org/10.1109/TGRS.2008.2000652.

Nelson, E. L., L'Ecuyer, T. S., Saleeby, S. M., Berg, W., Herbener, S. R., & Van Den Heever, S. C. (2016). Toward an algorithm for estimating latent heat release in warm rain systems. *Journal of Atmospheric and Oceanic Technology, 33*(6), 1309–1329. https://doi.org/10.1175/JTECH-D-15-0205.1.

Nesbitt, S. W., & Zipser, E. J. (2003). The diurnal cycle of rainfall and convective intensity according to three years of TRMM measurements. *Journal of Climate, 16*(10), 1456-1475. https://doi.org/10.1175/1520-0442(2003)016<1456:TDCORA>2.0.CO;2.

Radhakrishna, B., Satheesh, S. K., Narayana Rao, T., Saikranthi, K., & Sunilkumar, K. (2016). Assessment of DSDs of GPM-DPR with ground-based disdrometer at seasonal scale over Gadanki, India. *Journal of Geophysical Research: Atmospheres, 121*(19), 11792–11802.

https://doi.org/10.1002/2015JD024628.

Radhakrishna, B., Saikranthi, K., & Rao, T. N. (2020). Regional differences in raindrop size distribution within Indian subcontinent and adjoining seas as inferred from Global Precipitation Measurement Dual-frequency Precipitation Radar. *Journal of the Meteorological Society of Japan. Ser. II.*, *98*(3), 573–584. https://doi.org/10.2151/jmsj.2020-030.

Seela, B. K., Janapati, J., Lin, P. L., Wang, P. K., & Lee, M. T. (2018). Raindrop size distribution characteristics of summer and winter season rainfall over north Taiwan. *Journal of Geophysical Research: Atmospheres*, *123*(20), 11602–11624. https://doi.org/10.1029/2018JD028307.

Sekaranom, A. B., & Masunaga, H. (2019). Origins of heavy precipitation biases in the TRMM PR and TMI products assessed with CloudSat and reanalysis data. *Journal of Applied Meteorology and Climatology*, *58*(1), 37-54. https://doi.org/10.1175/JAMC-D-18-0011.1.

Seto, S., Iguchi, T., & Oki, T. (2013). The basic performance of a precipitation retrieval algorithm for the global precipitation measurement mission's single/dual-frequency radar measurements. *IEEE Transactions on Geoscience and Remote Sensing*, *51*(12), 5239–5251. https://doi.org/10.1109/TGRS.2012.2231686.

Seto, S., Shimozuma, T., Iguchi, T., & Kozu, T. (2016). Spatial and temporal variations of mass-weighted mean diameter estimated by GPM/DPR. Paper presented at *2016 IEEE International Geoscience and Remote Sensing Symposium*, Beijing, China. https://doi.org/10.1109/IGARSS.2016.7730023.

Skofronick-Jackson, G., Petersen, W. A., Berg, W., Kidd, C., Stocker, E. F., Kirschbaum, D. B., et al. (2017). The Global Precipitation Measurement (GPM) mission for science and society. *Bulletin of the American Meteorological Society*, *98*(8), 1679-1695. https://doi.org/10.1175/BAMS-D-15-00306.1.

Sohn, B. J., Choi, M. J., & Ryu, J. (2015). Explaining darker deep convective clouds over the western Pacific than over tropical continental convective regions. *Atmospheric Measurement Techniques*, *8*(11), 4573-4585. https://doi.org/10.5194/amt-8-4573-2015.

Sohn, B. J., Ryu, G.-H., Song, H.-J., & Ou, M.-L. (2013). Characteristic features of warm-type rain producing heavy rainfall over the Korean Peninsula inferred from TRMM measurements. *Monthly Weather Review*, *141*(11), 3873–3888. https://doi.org/10.1175/MWR-D-13-00075.1.

Song, H.-J., & Sohn, B. J. (2015). Two heavy rainfall types over the Korean peninsula in the humid East Asian summer environment: A satellite observation study. *Monthly Weather Review*, *143*(1), 363–382. https://doi.org/10.1175/MWR-D-14-00184.1.

Suh, S.-H., You, C.-H., & Lee, D.-I. (2016). Climatological characteristics of raindrop size distributions in Busan, Republic of Korea. *Hydrology and Earth System Sciences*, *20*(1), 193–207, https://doi.org/10.5194/hess-20-193-2016.

Sun, Y., Dong, X., Cui, W., Zhou, Z., Fu, Z., Zhou, L., et al. (2020). Vertical structures of typical Meiyu precipitation events retrieved from GPM-DPR. *Journal of Geophysical Research: Atmospheres, 125*(1). https://doi.org/10.1029/2019JD031466.

Takayabu, Y. N. (2002). Spectral representation of rain profiles and diurnal variations observed with TRMM PR over the equatorial area. *Geophysical Research Letters, 29*(12), 1584. https://doi.org/10.1029/2001GL014113.

Tang, Q., Xiao, H., Guo, C., & Feng, L. (2014). Characteristics of the raindrop size distributions and their retrieved polarimetric radar parameters in northern and southern China. *Atmospheric Research, 135*, 59–75. https://doi.org/10.1016/j.atmosres.2013.08.003.

Testud, J., Oury, S., Black, R. A., Amayenc, P., & Dou, X. (2001). The concept of "normalized" distribution to describe raindrop spectra: A tool for cloud physics and cloud remote sensing. *Journal of Applied Meteorology, 40*(6), 1118-1140. https://doi.org/10.1175/1520-0450(2001)040<1118:TCONDT>2.0.CO;2.

Thompson, E. J., Rutledge, S. A., Dolan, B., & Thurai, M. (2015). Drop size distributions and radar observations of convective and stratiform rain over the equatorial Indian and West Pacific Oceans. *Journal of the Atmospheric Sciences, 72*(11), 4091–4125. https://doi.org/10.1175/JAS-D-14-0206.1.

Tokay, A., & Short, D. A. (1996). Evidence from tropical raindrop spectra of the origin of rain from stratiform versus convective clouds. *Journal of applied meteorology, 35*(3), 355-371. https://doi.org/10.1175/1520-0450(1996)035<0355:EFTRSO>2.0.CO;2.

Ulbrich, C. W. (1983). Natural variations in the analytical form of the raindrop size distribution. *Journal of Climate and Applied Meteorology, 22*(10), 1764-1775. https://www.jstor.org/stable/26181251.

Ulbrich, C. W., & Atlas, D. (2007). Microphysics of raindrop size spectra: Tropical continental and maritime storms. *Journal of Applied Meteorology and Climatology, 46*(11), 1777–1791. https://doi.org/10.1175/2007JAMC1649.1.

Wen, L., Zhao, K., Chen, G., Wang, M., Zhou, B., Huang, H., et al. (2018). Drop size distribution characteristics of seven typhoons in China. *Journal of Geophysical Research: Atmospheres, 123*(12), 6529-6548. https://doi.org/10.1029/2017JD027950.

Williams, E., Rosenfeld, D., Madden, N., Gerlach, J., Gears, N., Atkinson, L., et al. (2002). Contrasting convective regimes over the Amazon: Implications for cloud electrification. *Journal of Geophysical Research: Atmospheres, 107*(D20), 8082. https://doi.org/10.1029/2001JD000380.

Wood, R., Bretherton, C. S., & Hartmann, D. L. (2002). Diurnal cycle of liquid water path over the subtropical and tropical oceans. *Geophysical Research Letters, 29*(23), 7-1. https://doi.org/10.1029/2002GL015371.

Xu, W., & Zipser, E. J. (2012). Properties of deep convection in tropical continental, monsoon, and oceanic rainfall regimes. *Geophysical Research Letters, 39*(7), L07802. https://doi.org/10.1029/2012GL051242.

Yamaji, M., Takahashi, H. G., Kubota, T., Oki, R., Hamada, A., & Takayabu, Y. N. (2020). 4-year climatology of global drop size distribution and its seasonal variability observed by spaceborne Dual-frequency Precipitation Radar. *Journal of the Meteorological Society of Japan. Ser. II.*. https://doi.org/10.2151/jmsj.2020-038.

Yang, S., & Smith, E. A. (2006). Mechanisms for diurnal variability of global tropical rainfall observed from TRMM. *Journal of Climate, 19*(20), 5190-5226. https://doi.org/10.1175/JCLI3883.1.

Zhang, G., Sun, J., & Brandes, E. A. (2006). Improving parameterization of rain microphysics with disdrometer and radar observations. *Journal of the Atmospheric Sciences, 63*(4), 1273-1290. https://doi.org/10.1175/JAS3680.1.

Zhang, G., Xue, M., Cao, Q., & Dawson, D. (2008). Diagnosing the intercept parameter for exponential raindrop size distribution based on video disdrometer observations: Model development. *Journal of Applied Meteorology and Climatology, 47*(11), 2983-2992. https://doi.org/10.1175/2008JAMC1876.1.

Zhang, Y., Wu, Z., Zhang, L., Xie, Y., Huang, Y., & Zheng, H. (2020). Preliminary study of land-sea microphysics associated with the East Asian Summer Monsoon rainband and its application to GPM DPR. *Journal of Atmospheric and Oceanic Technology, 37*(7), 1231–1249. https://doi.org/10.1175/JTECH-D-19-0059.1.

Zipser, E. J., Cecil, D. J., Liu, C., Nesbitt, S. W., & Yorty, D. P. (2006). Where are the most intense thunderstorms on Earth?. *Bulletin of the American Meteorological Society, 87*(8), 1057‑1072. https://doi.org/10.1175/BAMS-87-8-1057.

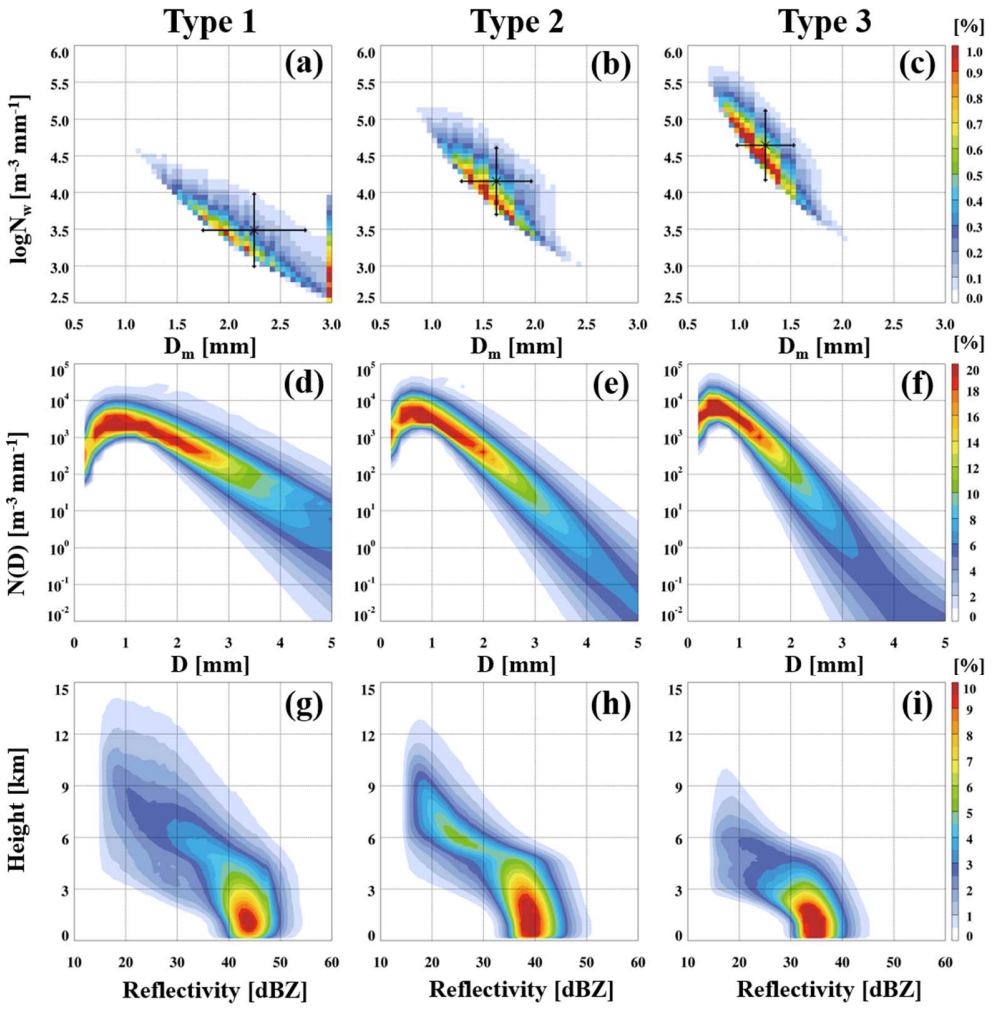

Figure 1. (a, b, c) Joint histograms of D_m and $logN_w$, and (d, e, f) histogram of calculated number concentration for the three DSD types of heavy rainfall. Black cross in the upper panel represents mean ± one standard deviation of D_m and $logN_w$. (g, h, i) Contoured frequency by altitude diagrams of Ku-band reflectivity for the three DSD types.

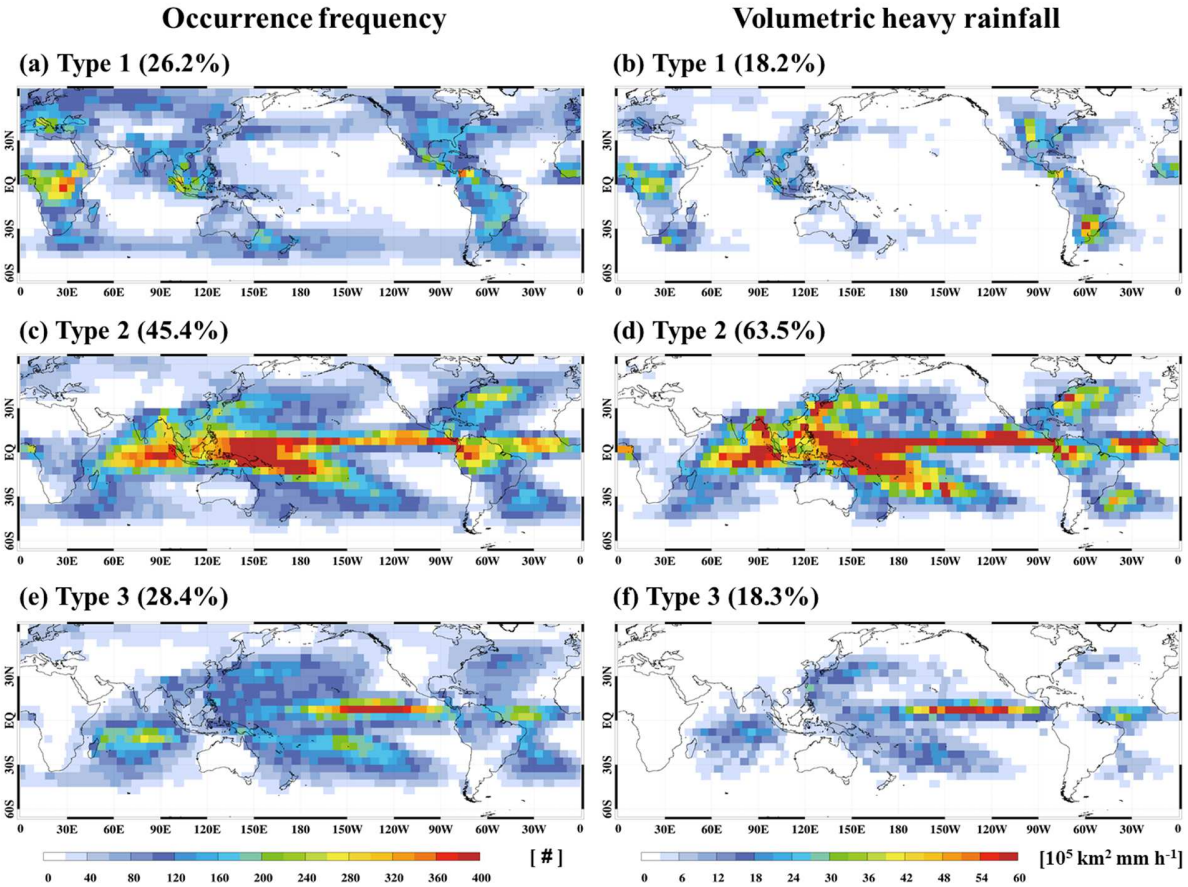

Figure 2. Spatial distributions of (a, c, e) occurrence frequency and (b, d, f) volumetric heavy rainfall for the three DSD types. Relative percentages of total occurrence and volumetric heavy rainfall are shown in each figure.

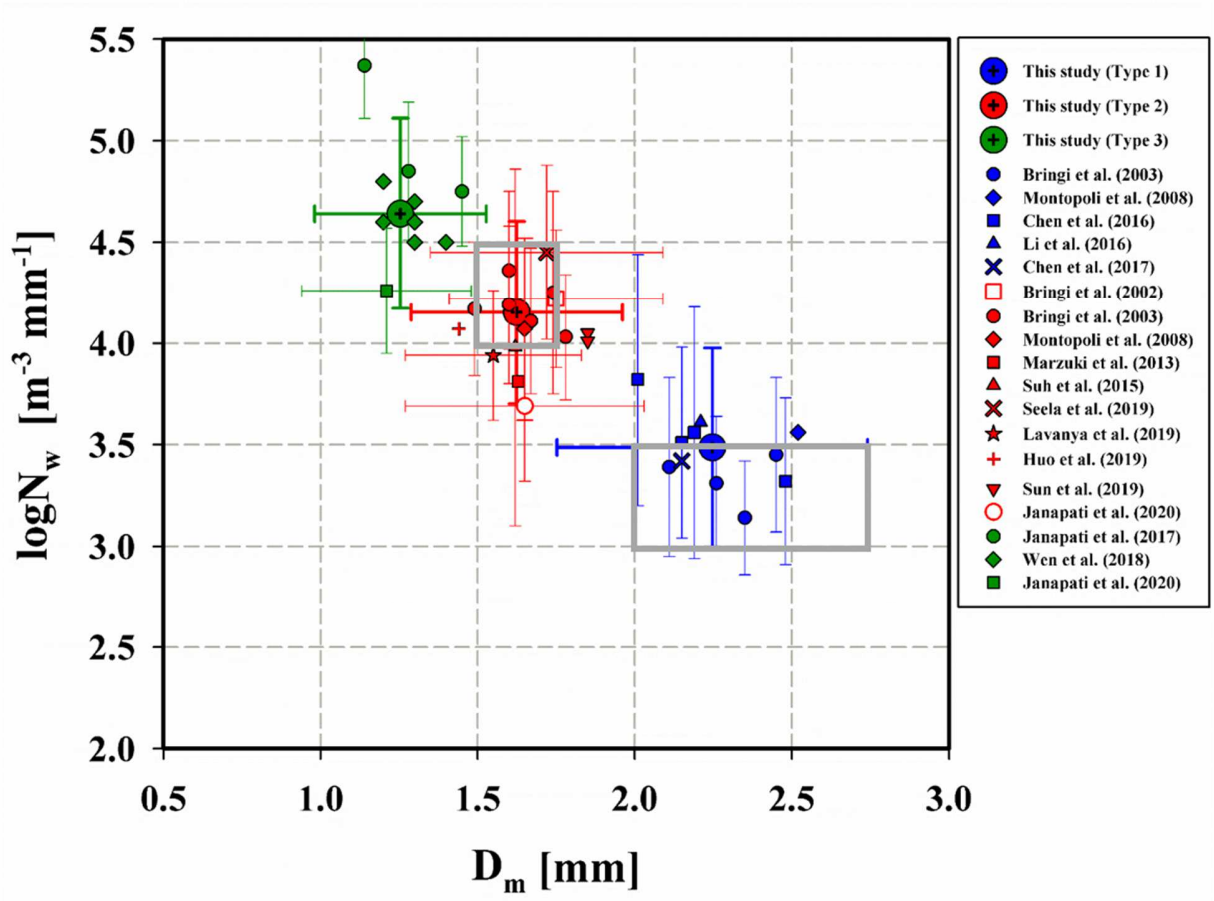

Figure 3. The global averages of D_m and $logN_w$ for the heavy rainfalls of the three DSD types categorized in this study (large dots) and average D_m and $logN_w$ measured in different regions as reported in previous studies (small symbols). Gray boxes represent continental and maritime convective clusters, as reported by Bringi et al. (2003). Detailed information is provided in Table S1.